Separation and Purification Technology 353 (2025) 128406

Contents lists available at ScienceDirect

Separation and Purification Technology

journal homepage: www.elsevier.com/locate/seppur

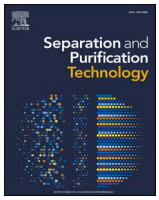

Kinetic study of magnesium dissolution using a magnesium oxide industrial by-product

V.B. Aguilar-Pozo [a,b], J.M. Chimenos [b], R. Soto [a], C. Da Silva [a], P. Botines [a], J.F. Izquierdo [a], S. Astals [a,*]

[a] Department of Chemical Engineering and Analytical Chemistry, University of Barcelona, 08028 Barcelona, Spain
[b] Department of Materials Science and Physical Chemistry, University of Barcelona, 08028 Barcelona, Spain

ARTICLE INFO

Editor: Xiyan Xu

Keywords:
Anaerobic digestion
Dissolution kinetics
Magnesium ammonium phosphate
Magnesium by-product
Magnesium oxide
Phosphorous recovery
Modelling
Struvite precipitation
Temperature
Wastewater treatment

ABSTRACT

Phosphorus recovery via struvite precipitation in wastewater treatment plants (WWTPs) is a key technology for nutrient recovery. This work investigates the dissolution kinetics of an industrial low-grade magnesium oxide (LG-MgO) by-product as an alternative to common magnesium sources for struvite precipitation. The main aims were to develop a parsimonious dissolution kinetic model capable of predicting the release of magnesium into the solution with accuracy and studying the influence of temperature on dissolution kinetics. The simultaneous fitting of all the experiments by non-linear regression rendered overall process values of the dissolution model's frequency factor (498,606 $L^{3.22}$ min^{-1} $mmol^{-1.74}$), activation energy (37.51 $kJ{\cdot}mol^{-1}$), and reaction order (2.74). The goodness-of-fit for all experiments was evaluated by the total sum of squared residuals and R^2 coefficients, being excellent under all conditions. The estimated kinetic coefficient values showed a temperature-dependent variation of the kinetic coefficient, increasing from 0.079 to 0.219 $L^{3.22}$ min^{-1} $mmol^{-1.74}$ when the temperature increased from 15 to 35 °C. The magnesium dissolution was fast in the first 5 min, where 40–78 % of magnesium dissolved with respect to the initial magnesium in the solid. Despite the assumptions made in the model derivation, the developed kinetic model provides a practical, reliable, and easy-to-use tool for WWTPs to estimate the LG-MgO dosage required to achieve targeted magnesium concentrations, thereby improving reagent use efficiency and phosphorus recovery.

1. Introduction

Phosphorus recovery via struvite precipitation is an emerging technology due to the need to recover this critical material while avoiding associated environmental problems. Currently, there are about 80 full-scale struvite precipitation plants in municipal and industrial wastewater treatment plants (WWTPs) worldwide [1]. However, this number is expected to increase rapidly since several countries (e.g. Germany and Switzerland) have enacted laws requiring phosphorous recovery in municipal WWTPs [2].

Struvite ($NH_4MgPO_4{\cdot}6H_2O$) is a valuable mineral that can be used as fertiliser due to its low impurity levels and slow release of nutrients [3,4]. Struvite precipitation could reduce phosphorus rock extraction since ~ 95 % of the phosphorus is used for fertiliser production worldwide [5]. Yuan et al. [6] estimated that phosphorous recovery as struvite from municipal sewage could meet 15–20 % of global phosphorous demand, reducing the need for phosphate rock exploitation. The struvite precipitation process in municipal WWTPs requires dosing a magnesium source and alkaline conditions [7,8]. Reagent consumption can account for as much as 75 % of the operational costs depending on the phosphorus concentration when using magnesium chloride (370 $€{\cdot}t^{-1}$) and sodium hydroxide (620 $€{\cdot}t^{-1}$) as reagents [9,10]. Accordingly, research on more cost-efficient alternative sources of magnesium has gained relevance to reduce struvite precipitation process operational costs [4,5,9,11].

Alternative magnesium sources for struvite precipitation include seawater, wood ash, spent refractory brick, magnesium oxide (MgO), and MgO by-products, among others [9,12–17]. Phosphorus recovery of over 90 % can be reached by using wood ash and seawater [15]. However, wood ash may contain a high heavy metal content, representing a problem for the final precipitate use as fertiliser [16], and seawater use is limited to WWTP located near the sea [9]. In addition, both wood ash and seawater require an additional dosage of alkaline reagent. Li et al. [18] used a leaching solution of spent refractory brick that contained

* Corresponding author.
E-mail address: sastals@ub.edu (S. Astals).

https://doi.org/10.1016/j.seppur.2024.128406
Received 22 March 2024; Received in revised form 27 May 2024; Accepted 11 June 2024
Available online 17 June 2024

high concentrations of calcium and magnesium. The precipitation conditions were a Mg:N:P molar ratio of 2:1:2 at pH 9.5, with 99.6 % of the phosphorus recovered as calcium phosphate and struvite. MgO is a basic oxide that can be used as both a magnesium source and an alkaline reagent. Reported phosphorus recoveries using reagent grade MgO range 80–90 % at pH 8.2–8.8 [19–21]. However, important drawbacks are the low solubility of MgO in water and the difficulties in controlling the release of magnesium ions (Mg^{2+}) given the strong dependence of its solubility on the solution pH [15]. The solubility of MgO increases with decreasing solution pH and increasing temperature [22,23]. Park et al. [15] studied the MgO dissolution in acid solutions (H_2SO_4, NH_4Cl, $NaHCO_3$ and others) and integrated these findings into the struvite precipitation model. The different acid solutions were an attempt to simulate the main protonic (H^+) species present in anaerobic digestion (AD) supernatants (NH_4^+, HCO_3^- and $H_2PO_4^-$) [15,18]. Park et al. [15] concluded that the MgO dissolution is governed by the H^+ concentration.

The application of low-grade magnesium oxide (LG-MgO) by-products from the calcination process of natural magnesite ($MgCO_3$) as a magnesium source and an alkaline reagent to precipitate struvite in WWTPs has already been addressed [12,13,24–29]. Quintana et al. [26] used LG-MgO to precipitate struvite in batch experiments, reporting phosphorus recovery from AD supernatant of 90 % after 240 min and pH of 8.6. Chimenos et al. [24] observed that a part of struvite was formed onto the LG-MgO particles, which served as both a magnesium source and a seed. Aguilar-Pozo et al. [27] reported a 75–85 % struvite content in the precipitate when using LG-MgO for P:Mg molar ratios of 1:0.5, 1:1 and 1:3. Quintana et al. [30] used a first-order kinetic model to describe struvite precipitation when using a LG-MgO by-product. However, the rate coefficient and equilibrium concentration varied with the added amount of by-product, requiring to adjust the model constants based on the P:Mg molar ratio. This suggests that other reaction orders should be considered since, under the theoretical basis rate coefficients are solely dependent on temperature. The comprehension of the factors controlling the dissolution of LG-MgO could lead to develop more general and realistic models, disentangling the rate constants dependence on the MgO and LG-MgO concentration.

The main objective of this study is to develop a simple, practical and parsimonious kinetic model that can accurately predict (i) the magnesium concentration over time, and (ii) the influence of temperature on the LG-MgO dissolution. Accordingly, the model should be able to render the amount of LG-MgO required to achieve targeted Mg^{2+} concentrations, such as those required in the struvite precipitation process.

2. Materials and methods

2.1. Magnesium oxide by-product origin and composition

The low-grade magnesium oxide (LG-MgO) by-product used was supplied by Magnesitas Navarras, S.A. (Navarra, Spain). The LG-MgO was collected from the cyclones and fabric filters of a rotatory kiln during the calcination of natural magnesite. Within the rotary kiln, the fine particles are dragged by flue gases to the gas treatment units throughout the combustion process. The calcination process determines certain properties of the LG-MgO, e.g. particle size distribution (PSD), composition, and reactivity. The LG-MgO was mainly composed of MgO (47.8 wt%) but also contains other mineral phases, including 21.7 wt% $MgCO_3$, 10.4 wt% $CaCO_3$, 5.7 wt% $CaMg(CO_3)_2$, 2.9 wt% $Mg(OH)_2$, and small amounts of Al_2O_3, $CaSO_4$, Fe_2O_3, $MgSO_4$, and SiO_2. The mineral composition was estimated by combining characterisation information from X-ray fluorescence (XRF, Philips PW2400 sequential wavelength-dispersive X-ray fluorescence spectrophotometer) (Table A1), X-ray diffraction (XRD, Bragg-Brentano PANalytical X'Pert PRO MPD) (Fig. 4a) and thermogravimetric analysis (TGA, SDT Q600 Simultaneous TGA204 DSC) [12,31]. The porosity of the LG-MgO was 0.5, which was measured using a Micrometrics Tristar 3000 porosimeter with the BET single-point method. The mean diameter (d_{50}) was 22.7 μm, as determined by the PSD using a Beckman Coulter LS 13320 laser diffraction particle size analyser. The LG-MgO particles exhibited a relatively narrow unimodal PSD (Fig. A1). The morphology of the LG-MgO was analysed using scanning electron microscopy (SEM) with a Quanta 200 FEI scanning electron microscope. The particles displayed irregular morphology (Fig. A2), with some being more elongated and others chunkier. However, their elongation ratio is generally not significant enough to prevent them from being approximated as sphere-like bodies. Aguilar-Pozo et al. [12] provide a complete characterisation of the LG-MgO used in this research, referred to as LG-MgO_B.

The acid neutralisation capacity (ANC) test was used to determine the buffering capacity of the LG-MgO [32]. Fig. 1 shows the ANC curve for the LG-MgO used in this study, which can be divided into three stages. Stage 1 ($11.1 > pH > 10.5$) is controlled by the dissolution equilibrium of $Mg(OH)_2$. Stage 2 ($10.5 > pH > 8.5$) is mainly dominated by the dissolution equilibrium of MgO. Stage 3 ($8.5 > pH > 4.3$) is governed by the CO_3^{2-}/HCO_3^- equilibrium from the presence of magnesium and calcium carbonates within the by-product. The ANC curve shows that the dissolution equilibrium of MgO predominantly controls the buffering capacity of LG-MgO. Protons were primarily consumed by the MgO phase and by the $Mg(OH)_2$ phase. The CO_3^{2-}/HCO_3^- equilibrium represented about 9 % of the total proton consumption.

2.2. Anaerobic digestion supernatant and synthetic supernatant solution

The anaerobic digestion supernatant was obtained from a full-scale mesophilic anaerobic digester located in a WWTP in Navarra (Spain) with a population equivalent treatment capacity of about 750.000. Table 1 shows the characterisation of the supernatant.

The synthetic supernatant solution was prepared using deionised water, anhydrous citric acid ($C_6H_8O_7$, Merck Sigma-Aldrich) to provide buffer capacity and sodium hydroxide (NaOH, PanReac AppliChem) to adjust pH. Citric acid is a triprotic organic acid thus exhibiting three pKa values (3.1, 4.8, and 6.4, respectively) [33]. Two different citric acid concentrations were used: (i) 0.1 $mol \cdot L^{-1}$ for LG-MgO additions below 1 $g \cdot L^{-1}$, and (ii) 1 $mol \cdot L^{-1}$ for LG-MgO additions greater than or equal to 1 $g \cdot L^{-1}$. Subsequently, a 2 $mol \cdot L^{-1}$ NaOH solution was added dropwise to increase the pH to 5.5, allowing the buffer capacity of the dissociation reaction equilibrium to be used in the aqueous suspension of LG-MgO (Eq. (1)).

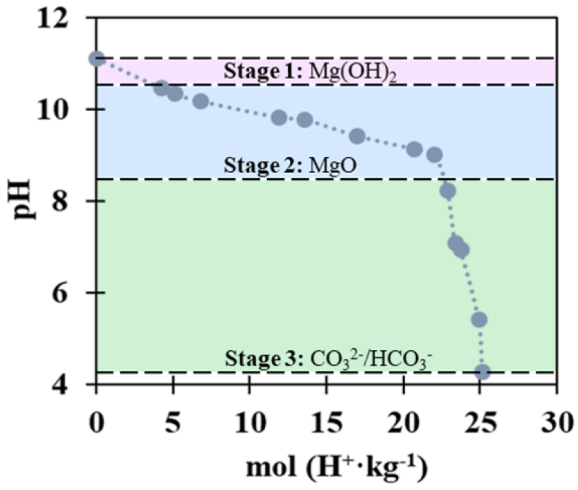

Fig. 1. Acid neutralisation capacity curve of the LG-MgO. Horizontal dashed lines delimit the stages that control the dissolution equilibrium.

Table 1
Characterisation of the anaerobic digestion supernatant.

Parameters	Units	Values
PO_4-P	mg $P{\cdot}L^{-1}$	132
Cl^-	mg$\cdot L^{-1}$	562
SO_4^{2-}	mg$\cdot L^{-1}$	24
Mg^{2+}	mg$\cdot L^{-1}$	36
TAN†	mg $N{\cdot}L^{-1}$	1356
Ca^{2+}	mg$\cdot L^{-1}$	160
Na^+	mg$\cdot L^{-1}$	70
K^+	mg$\cdot L^{-1}$	338
pH	–	7.9
Partial Alkalinity	mg $CaCO_3{\cdot}L^{-1}$	3483
Total Alkalinity	mg $CaCO_3{\cdot}L^{-1}$	4465

† TAN: total ammoniacal nitrogen.

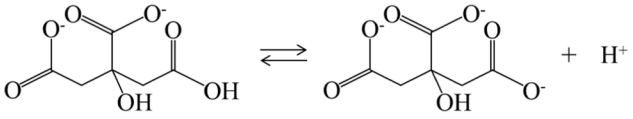

(1)

The synthetic solution used to assess the dissolution of LG-MgO particles kept the pH of the solution well below the MgO equilibrium pH of 10.5 to prevent equilibrium limitations that would limit the continuous release of Mg into the medium [34].

2.3. Experimental set-up

2.3.1. LG-MgO dissolution in anaerobic digestion supernatant

The magnesium dissolution trials in AD supernatant were carried out in duplicate using a jar test device (Velp Scientifica® JT6) and beakers containing 0.5 L of useful solution volume, under continuous mixing at 200 rpm for 70 min at room temperature (ca. 20 °C). The LG-MgO added was 1.1 $g{\cdot}L^{-1}$, corresponding to a P:Mg molar ratio of 1:4. During the experiments, 6 mL aliquots were sampled at 0, 5, 10, 20, 40, and 70 min, which were immediately filtered using a 0.22 μm regenerated cellulose syringe filter. Subsequently, the pH and Mg concentrations were measured by a micro pH electrode and an ionic chromatograph, respectively. The main objective of this experiment was to show the continuous release of magnesium from LG-MgO when used in the anaerobic digestion supernatant.

2.3.2. LG-MgO dissolution in a synthetic solution

The magnesium dissolution trials in synthetic solution were performed in two identical 4 L jacketed glass reactors used as technical duplicates, under continuous mixing at 200 rpm by paddle overhead agitators. The isothermal conditions (±0.2 °C) were ensured by circulating water through the reactor jacket from a thermostatic bath (CORIO CBT9).

The dissolution kinetics were studied at five different LG-MgO concentrations (i.e. 0.25, 0.375, 0.50, 1.00 and 2.50 $g{\cdot}L^{-1}$) and three different temperatures (i.e. 15, 25 and 35 °C), resulting in a total of fifteen different experimental conditions with their replicates. The LG-MgO concentrations of 0.25, 0.375, 0.50, 1.0 and 2.50 $g{\cdot}L^{-1}$ correspond to P:Mg molar ratios of 1:1, 1:1.5, 1:2, 1:4 and 1:10, respectively, considering that phosphorus concentration in the supernatant is 120 $mg{\cdot}L^{-1}$. Each experiment comprised 2 L of synthetic solution (0.1 $mol{\cdot}L^{-1}$ for LG-MgO additions < 1 $g{\cdot}L^{-1}$, and 1 $mol{\cdot}L^{-1}$ for LG-MgO addition ≥ 1 $g{\cdot}L^{-1}$) and lasted for 60 min. To monitor the LG-MgO dissolution kinetics, 6 mL aliquots were sampled at 0, 5, 10, 15, 20, 25, 30, 40, 50 and 60 min, which were immediately filtered using a 0.22 μm regenerated cellulose syringe filter. The pH and Mg concentration were measured in duplicate by a micro pH electrode and an ionic chromatograph, respectively.

2.4. Analytical methods

pH was measured with a micro pH electrode PHEL-GB3-001 connected to a MultiMeter MM41 (Crison). The Mg concentration was measured using an ionic chromatographer 861 Advanced Compact IC Metrohm equipped with a Metrosep column from cation analysis (Metrosep A Supp 17–250/4.0). The mobile phase is a solution containing 1.7 $mmol{\cdot}L^{-1}$ of nitric acid and 0.7 $mmol{\cdot}L^{-1}$ of dipicolinic acid in ultrapure water, resulting in a pH of 2.6. It should be noted that any complexation between magnesium and citrate would be decomplexed by the low pH of the mobile phase.

After each run, the remaining undissolved solids were analysed by XRD and TGA techniques. XRD was carried out using a Bragg-Brentano PANalytical X'Pert PRO MPD alpha1 powder diffractometer with $CuK_{\alpha 1}$ radiation ($\lambda = 1.5406$ Å) focalising Ge (1 1 1) primary monochromator, ranging from 4 to 100° (2θ-angle) with a step size of 0.026° and measuring time of 100 s. The X'Pert HighScore software was used to identify the crystalline mineral phases of the solids. TGA was conducted using an SDT-Q600 Simultaneous TGA204 DSC (TA Instruments) under an inert N_2 gas atmosphere. The temperature-controlled program consisted of a heating rate of 10 $°C{\cdot}min^{-1}$ within a temperature ranging from 30 to 1200 °C. TGA was used to quantify the weight loss percentage of each mineral phase ($Mg(OH)_2$, $MgCO_3$, $CaMg(CO_3)_2$ and $CaCO_3$) through their thermal decomposition reaction (Eq. (2)–(5)).

$$Mg(OH)_2(s) \rightarrow MgO(s) + H_2O(g) \quad (2)$$

$$MgCO_3(s) \rightarrow MgO(s) + CO_2(g) \quad (3)$$

$$CaMg(CO_3)_2(s) \rightarrow MgO(s) + CaO(s) + 2\ CO_2(g) \quad (4)$$

$$CaCO_3(s) \rightarrow CaO(s) + CO_2(g) \quad (5)$$

2.5. Empirical kinetic model for MgO dissolution

The MgO dissolution in an acid medium illustrates a liquid–solid dissociation reaction of an ionic solid. The process involves the consecutive steps of external mass transfer and dissociation reaction. In this context, external mass transfer refers to the diffusion of H^+ from the bulk solution through the film to the particle surface, as well as the reverse diffusion of ionic reaction products from the solid surface to the bulk liquid. The dissociation reaction, or ionisation reaction of the solid, takes place on the particle surface as a result of the solute–solvent molecular interactions, resulting in the production of magnesium ions and water (Eq. (6)).

$$MgO(s) + 2H^+(aq) \rightarrow Mg^{2+}(aq) + H_2O(l) \quad (6)$$

Bugajski et al. [35], Fedoročková et al. [23] and Raschman et al. [36] proposed a kinetic model for MgO dissolution in an acidic medium, where the rate of reaction is described by a power-law function of the activity or concentration of H^+. Raschman et al. [36] concluded that the MgO dissolution is controlled by the chemical reaction since the estimated kinetic coefficient was three orders of magnitude lower than the external mass transfer coefficient. In this study, a MgO by-product containing other alkaline phases was used (e.g. $CaCO_3$). These additional phases can also consume H^+ in the acidic medium, thereby affecting the activity or concentration of H^+ used in the kinetic model of MgO dissolution. Therefore, the model derivation was based on the monitoring of Mg solution concentration. Moreover, the proposed parsimonious empirical kinetic model considers the following assumptions:

- The dissolved magnesium comes from the MgO and $Mg(OH)_2$ phases, and the $Mg(OH)_2$ dissolution is very similar to that for the MgO [37].

- In an acid medium with excess H^+, MgO does not reach equilibrium and the MgO particles undergo dissolution.
- The reaction rate (r) is related to the undissolved Mg from the LG-MgO (reactant).
- The apparent kinetic coefficient (k*) includes the H^+ concentration, which is assumed to be constant (excess reactant) throughout the experiment due to the buffered solution. It also includes information regarding the reduction of particles' surface area over time caused by dissolution.

The reaction rate of the magnesium contained in the LG-MgO is expressed as a power-law and describes the variation of Mg concentration ($c_{Mg(s)}$) in the LG-MgO particles over time (Eq. (7)). The derivation of this equation is based on the diffusion–reaction theory [33], which considers dissolution to be a two-step process in series: the surface reaction triggers the detachment of magnesium molecules from the solid surface, followed by the diffusion from the solid surface to the bulk solution via the film boundary layer. The latter is known to depend on the mass transfer coefficient showing, a linear relation with temperature, while the surface reaction often exhibits higher reaction orders concerning the dissolution of some salts [38]. When the concentration range covered by the dissolution experiment is far from equilibrium, the solubility is not considered in the driving force, and, consequently, the reaction rate only depends on the actual concentration.

$$\frac{dc_{Mg(s)}}{dt} = r = -\frac{k^*}{c_{Mg(s),0}} \cdot c_{Mg(s)}^{\beta} \tag{7}$$

where β is the reaction order and $c_{Mg(s),0}$ is the initial Mg concentration of the LG-MgO.

Since five different concentrations of LG-MgO were studied, the inclusion of $c_{Mg(s),0}$ in the model is considered appropriate. This normalisation of rate values ensures that all experiments have the same weight during the regression process, minimising the sum of squares errors. The apparent kinetic coefficient (k*) entails the contribution of the true rate coefficient, which depends on temperature following an Arrhenius–like equation (Eq. (8)). Additionally, it considers the change in surface area with time (A) caused by particle dissolution and the assumed virtually constant protons concentration according to the excess reactant simplified kinetics. Here, $A^*_0 = A_0 \bullet A \bullet c_{H+}$ where A_0 is the frequency (pre-exponential).

$$k^* = A^*_0 \cdot e^{\left(\frac{-E_a}{R \cdot T}\right)} \tag{8}$$

where A^*_0 is the apparent frequency (pre-exponential) factor and E_a is the apparent activation energy (kJ·mol^{-1}), R denotes the gas constant (0.0083 J·k^{-1}·mmol^{-1}) and T is the absolute temperature (K).

Combining Eq. (7) and (8), a general kinetic expression is obtained (Eq. (9)):

$$\frac{dc_{Mg(s)}}{dt} = -\frac{A^*_0 \cdot e^{\left(\frac{-E_a}{R \cdot T}\right)}}{c_{Mg(s),0}} \cdot c_{Mg(s)}^{\beta} \tag{9}$$

The integration of Eq. (9) results in Eq. (10), which expresses the Mg concentration change in the LG-MgO over time (t). In Eq. (10), t_0 is the initial time that is 0.

$$\frac{c_{Mg(s)}{}^{-\beta+1}}{-\beta+1} - \frac{c_{Mg(s),0}{}^{-\beta+1}}{-\beta+1} = -\frac{A^*_0 \cdot e^{\left(\frac{-E_a}{R \cdot T}\right)}}{c_{Mg(s),0}} (t - t_0) \tag{10}$$

Finally, Eq. (11) relates the Mg concentrations in the solid and the liquid. The Mg concentration in the medium over time (c^{2+}_{Mg}) is the difference between the initial Mg concentration in the LG-MgO and the Mg concentration in the LG-MgO over time ($c_{Mg(s),0} - c_{Mg(s)}$).

$$C_{Mg^{2+}} = c_{Mg(s),0} - \left(c_{Mg(s),0}{}^{-\beta+1} - \frac{A^*_0 \cdot e^{\left(\frac{-E_a}{R \cdot T}\right)}}{c_{Mg(s),0}} t \cdot (-\beta+1) \right)^{1/(-\beta+1)} \tag{11}$$

Eq. (11) has been fitted simultaneously for all experimental results using Excel, enabling the estimation of β, A^*_0, and E_a. This was achieved through a non-linear regression, involving the minimisation of the sum of squared residuals (SSR) between the experimental and estimated Mg concentrations at different conditions (i.e. LG-MgO initial concentration and temperature). To ensure the convergence at a global minimum, the initial values for the estimates were varied over several orders of magnitude.

It should be noted that the apparent pre-exponential factor represents the lumped product group of constants $A_0 \bullet A \bullet c_{H+}$ since separating individual contributions is unadvisable due to the high correlation between estimates. Accordingly, the reported estimated values must be interpreted with caution, as they are specific to the surface area values related to the particle size features of the LG-MgO by-product used in this study. In other words, if the dissolution model attempts to be used for other particle sizes, different parameters to those estimated in this research must be determined.

The sphere-shrinking model has yielded reasonably good results in modelling the dissolution kinetics of some salts [39]. Nonetheless, the resulting mathematical expression is considerably more complex making its application unjustifiable for certain purposes. LG-MgO is a by-product with heterogeneous characteristics in shape, size, and composition that can influence the dissolution kinetics. Therefore, it was decided to simplify the study and consider certain constant parameters that are included in the estimated values, such as the variation of the surface area over time. The aim of modelling the dissolution kinetics is to provide a simple, practical, and parsimonious model capable of predicting the Mg concentration with high accuracy while avoiding overparameterisation.

3. Results and discussion

3.1. Dissolution of LG-MgO in anaerobic digestion supernatant

The dissolution of 1.1 g·L^{-1} of LG-MgO in AD supernatant is shown in Fig. 2, where the Mg concentration and pH increased to 134 ± 2 mg·L^{-1} and 8.67 ± 0.01, respectively. The impact of phosphorous precipitation in these experiments can be disregarded because magnesium was added in excess (molar ratio P:Mg 1:4). The buffering capacity of AD

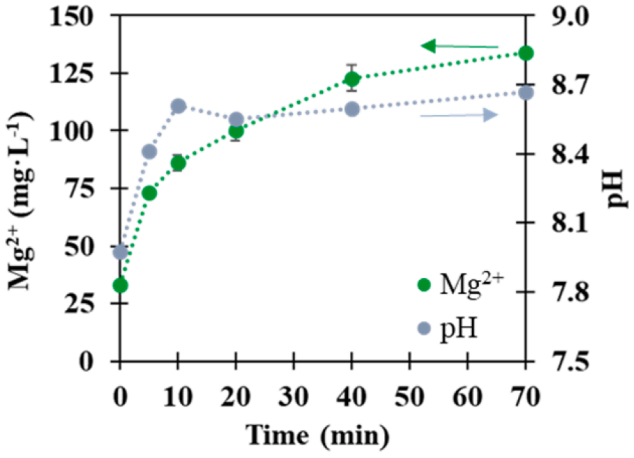

Fig. 2. Evolution of pH and Mg^{2+} concentration over time for the LG-MgO dissolution in anaerobic digestion supernatant. Reading direction: left Mg^{2+} concentration (←) and right pH (→).

supernatant, mainly due to HCO_3^- and CO_3^{2-} species, limited the pH increase, promoting the continuous release of Mg^{2+} from LG-MgO into the medium. These results confirmed the suitability of LG-MgO as a magnesium source and as an alkaline reagent for struvite precipitation. However, the effective use of LG-MgO and dosing strategies design require gaining further understanding on the dissolution kinetics. The kinetic study in the supernatant AD would impede the measurement of the real concentration of dissolved magnesium, as it can precipitate with phosphates and carbonates. This would result in a lower measured magnesium concentration than the actual amount present. Accordingly, the dissolution kinetic experiments were carried out in a synthetic supernatant solution.

3.2. LG-MgO dissolution in a synthetic supernatant solution

The dissolution of LG-MgO particles in a synthetic acid solution showed a continuous release of Mg^{2+} from LG-MgO, with pH values far from equilibrium (pH ≪ 10.5) (Fig. 3). This behaviour is similar to that observed for the dissolution of LG-MgO in AD supernatant (Fig. 2). The dissolution rate of LG-MgO increased with temperature, resulting in higher Mg^{2+} and hydroxide (OH^-) concentrations in the medium. These results are consistent with previous MgO dissolution studies [22,40]. The Mg^{2+} released during the first 5 min of the experiments shows a notable dependence on temperature and accounted for approximately 40–78 % of the magnesium contained in the LG-MgO. After this initial 5 min period, the release of Mg^{2+} proceeded at a slower rate.

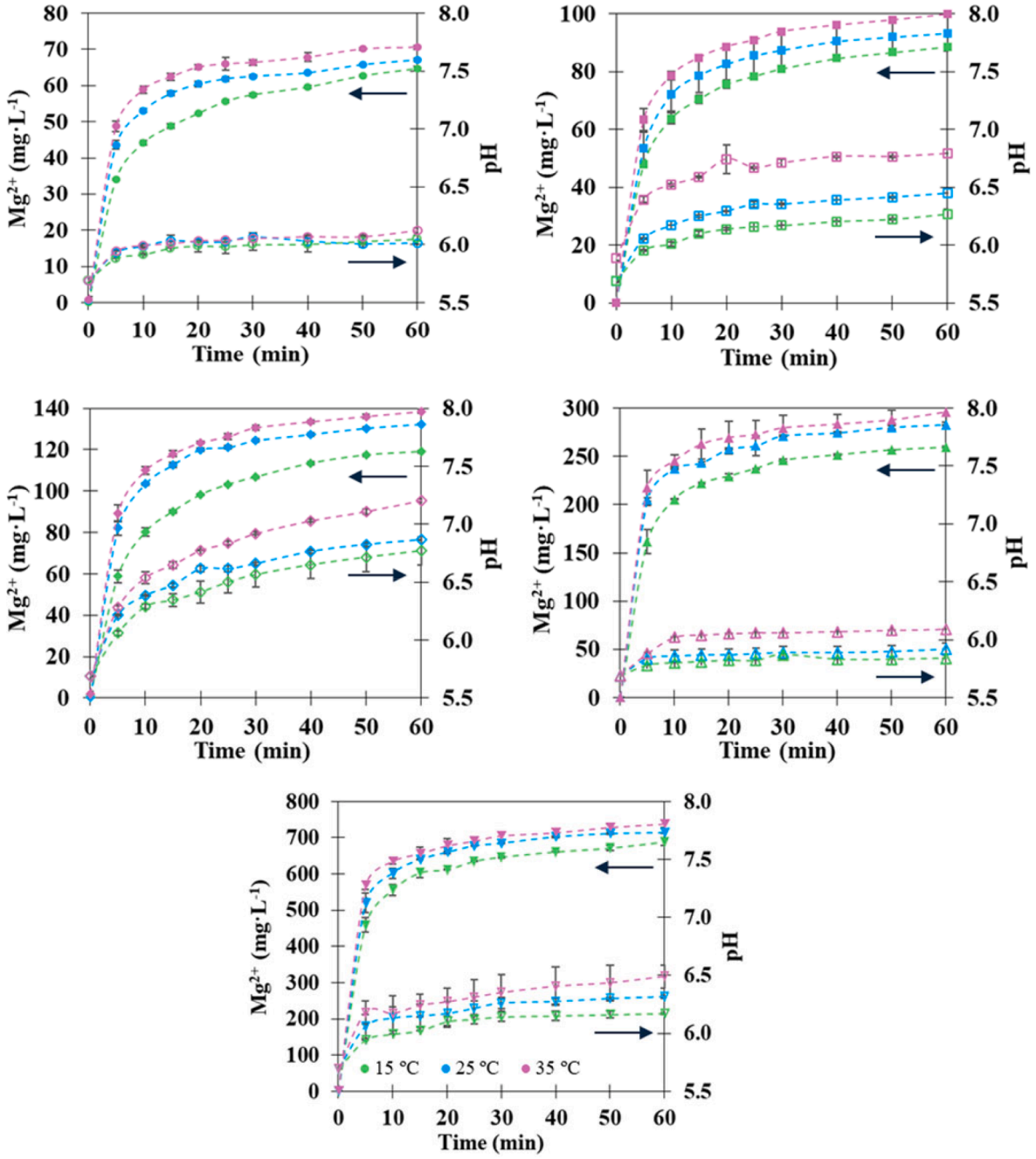

Fig. 3. Dissolution in synthetic solution at different LG-MgO concentrations (●) 0.25 g·L^{-1}, (■) 0.375 g·L^{-1}, (◆) 0.50 g·L^{-1}, (▲) 1.00 g·L^{-1} and (▼) 2.50 g·L^{-1}. (●) Mg^{2+} concentration and (○) pH over time for each LG-MgO initial concentration Temperature of (●) 15 °C, (●) 25 °C and (●) 35 °C. Dashed lines are a guide for the eye. Reading direction: left Mg^{2+} concentration (←) and right pH (→).

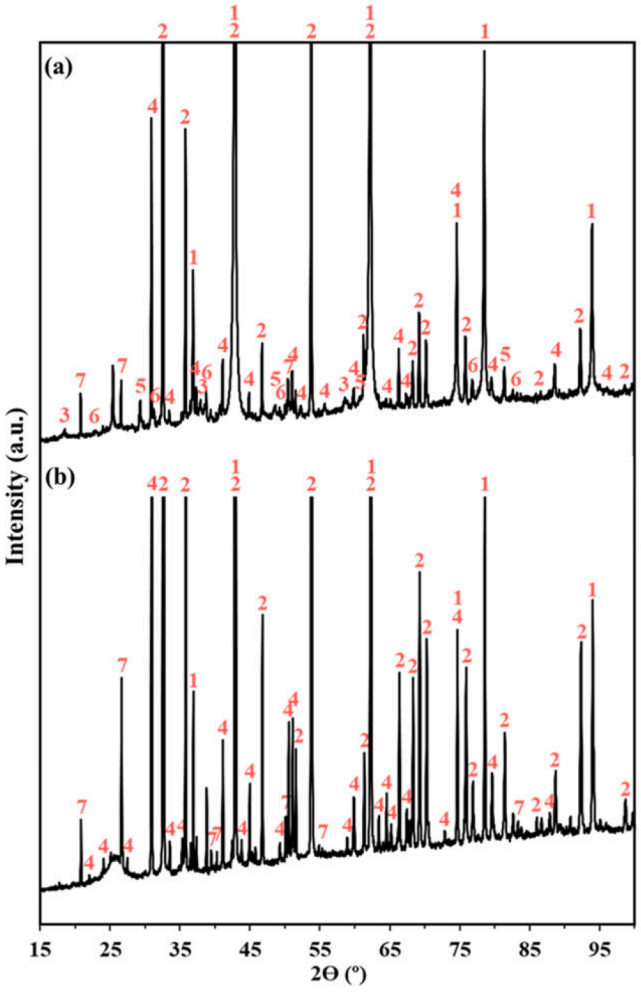

Fig. 4. X-ray diffractograms of the (a) LG-MgO raw material and (b) undissolved solid fraction (experiment: 2.50 g·L^{-1} of LG-MgO and 15 °C). Mineral phases: (1) MgO, (2) $MgCO_3$, (3) $Mg(OH)_2$, (4) $MgCa(CO_3)_2$, (5) $CaCO_3$, (6) $CaSO_4$ and (7) SiO_2.

Fig. 3 illustrates the Mg^{2+} concentration and pH trend at different LG-MgO concentrations. Specifically, the Mg^{2+} concentrations at 35 °C after 60 min were 70.6 ± 0.6, 99.8 ± 0.5, 138 ± 1, 295 ± 11 and 738 ± 13 mg·L^{-1} when the initial LG-MgO concentration was 0.25, 0.375, 0.50, 1.00 and 2.50 g·L^{-1}, respectively. The dissolution of LG-MgO in deionised water showed an opposite trend, i.e. the higher the concentration of LG-MgO in deionised water, the lower the Mg^{2+} released [12]. The dissolution of LG-MgO in deionised water was limited by equilibrium since the pH of the solution reached 10.7 due to the lack of buffer capacity in deionised water [12]. The solution of 0.1 mol·L^{-1} acid citric used in LG-MgO additions of 0.25, 0.375 and 0.50 g·L^{-1} evidenced that pH increased with the addition of LG-MgO and time (Fig. 3a-c). pH values around 7.3 were reached when working with LG-MgO additions of 0.50 g·L^{-1}, which is close to the citric acid buffer breakthrough (pK_{a3} = 6.4). To provide enough alkalinity to the system, a 1 mol·L^{-1} citric acid solution was used for LG-MgO concentrations of 1.00 and 2.50 g·L^{-1}, increasing the solution medium with a higher buffering capacity (Fig. 3d-e). For these LG-MgO concentrations, the maximum pH value recorded was 7.2 (Fig. 3d-e).

3.2.1. Characterisation of the LG-MgO before and after dissolution

The mineral phases of the raw LG-MgO were MgO, $MgCO_3$, $Mg(OH)_2$, $MgCa(CO_3)_2$, $CaCO_3$, $CaSO_4$ and SiO_2 (Fig. 4a). These mineral phases are typical of industrial MgO by-products from natural magnesite calcination, where MgO is the main mineral phase, followed by $MgCO_3$ and $CaCO_3$ [12,31,32]. After the dissolution experiments, the solid fraction collected had $MgCO_3$, MgO and $MgCa(CO_3)_2$ as main mineral phases. The presence of $Mg(OH)_2$, $CaCO_3$, and $CaSO_4$ (Fig. 4b) was not detected. These results indicate that these mineral phases either dissolved in the acid solution or were present in quantities below the quantification limit of the XRD equipment. No diffraction bands were present between the theta angle 0–15°.

The weight loss of the solid harvested after dissolution experiments, compared to the initial mass of LG-MgO added, ranged from 43 to 45 wt %. In a specific representative run (2.5 g·L^{-1} and 15 °C), a total solid mass of 2.25 ± 0.21 g was collected out of the initial amount of LG-MgO added of 5.00 ± 0.01 g. TGA analysis of the collected solids revealed that the percentages of $MgCO_3$ and $MgCa(CO_3)_2$ doubled compared to the initial LG-MgO composition (Table 2). In the same specific representative run, 1.11 ± 0.10 g of $MgCO_3$ and 0.26 ± 0.02 g of $MgCa(CO_3)_2$ were collected after the experiment, compared to the 1.10 g of $MgCO_3$ and 0.29 g of $MgCa(CO_3)_2$ present at the beginning of the experiment. Therefore, the amount of magnesium dissolved from carbonate mineral phases can be considered negligible and the magnesium carbonates presented in LG-MgO were classified as unreactive phases. In other words, the predominant source of the Mg^{2+} was MgO, with a minor contribution from $Mg(OH)_2$. These observations are evidence confirming that the dissolved Mg^{2+} arises from the MgO and $Mg(OH)_2$ phases. The remaining solid contained 2.36 wt% of $Mg(OH)_2$ after dissolution, indicating a three-fold reduction of this with respect to the initial concentration. The $CaCO_3$ phase was never detected in the undissolved solid, suggesting its complete dissolution in the acidic solution.

3.3. Empirical kinetic modelling

The estimates of β, A^*_0 and E_a were 2.74, 498,606 $L^{3.22}\cdot min^{-1}\cdot mmol^{-1.74}$ and 37.5 kJ·mol^{-1}, respectively. These model parameters (β, A^*_0 and E_a) were estimated from the collected pool of experimental data using Eq. (11). As illustrated in Fig. 5, and excellent prediction capability of the model developed is observed, evidenced by nearly identical values of the experimentally measured and estimated Mg^{2+} concentrations (Fig. 6a). The simultaneous fit of all experiments yielded very high coefficients of determination ($R^2 > 0.99$). The individual fitting of each experiment also resulted in remarkably high R^2 values, always above 0.99 (Table A2). These outcomes demonstrate the excellent prediction capability of the model derived from the values estimated to explain the experimental reality observed. This conclusion is further supported by the random and even distribution of residuals discarding the presence of hidden systematic errors on the measurements or hidden mathematical artifacts from the modelling derivation, and also by the almost perfect distribution of values across the parity plot diagonal. As indicative figures, the estimated parameters enabled the calculation of kinetic coefficients at 15, 25 and 35 °C are 0.079, 0.134 and 0.219 $L^{3.22}\cdot min^{-1}\cdot mmol^{-1.74}$, respectively. An immediate aftermath from such values is the confirmation of dissolution kinetics featured by rate values increasing with temperature, as expected from the Arrhenius-like temperature relation of the coefficients. This is particularly noticeable during the first 5 min of dissolution (Fig. 5). After

Table 2
The decomposition temperature range and weight loss percentage of $Mg(OH)_2$, $MgCO_3$, $CaMg(CO_3)_2$ and $CaCO_3$ present in the initial LG-MgO and the undissolved solid (experiment: 2.50 g·L^{-1} and 15 °C).

Species	LG-MgO(wt %)	Undissolved solid (wt %)	Temperature ranges (°C)
$Mg(OH)_2$	7.71	2.36	204—420
$MgCO_3$	22.05	49.43	420—640
$CaMg(CO_3)_2$	5.82	11.45	640—780
$CaCO_3$	10.53	0	780—970

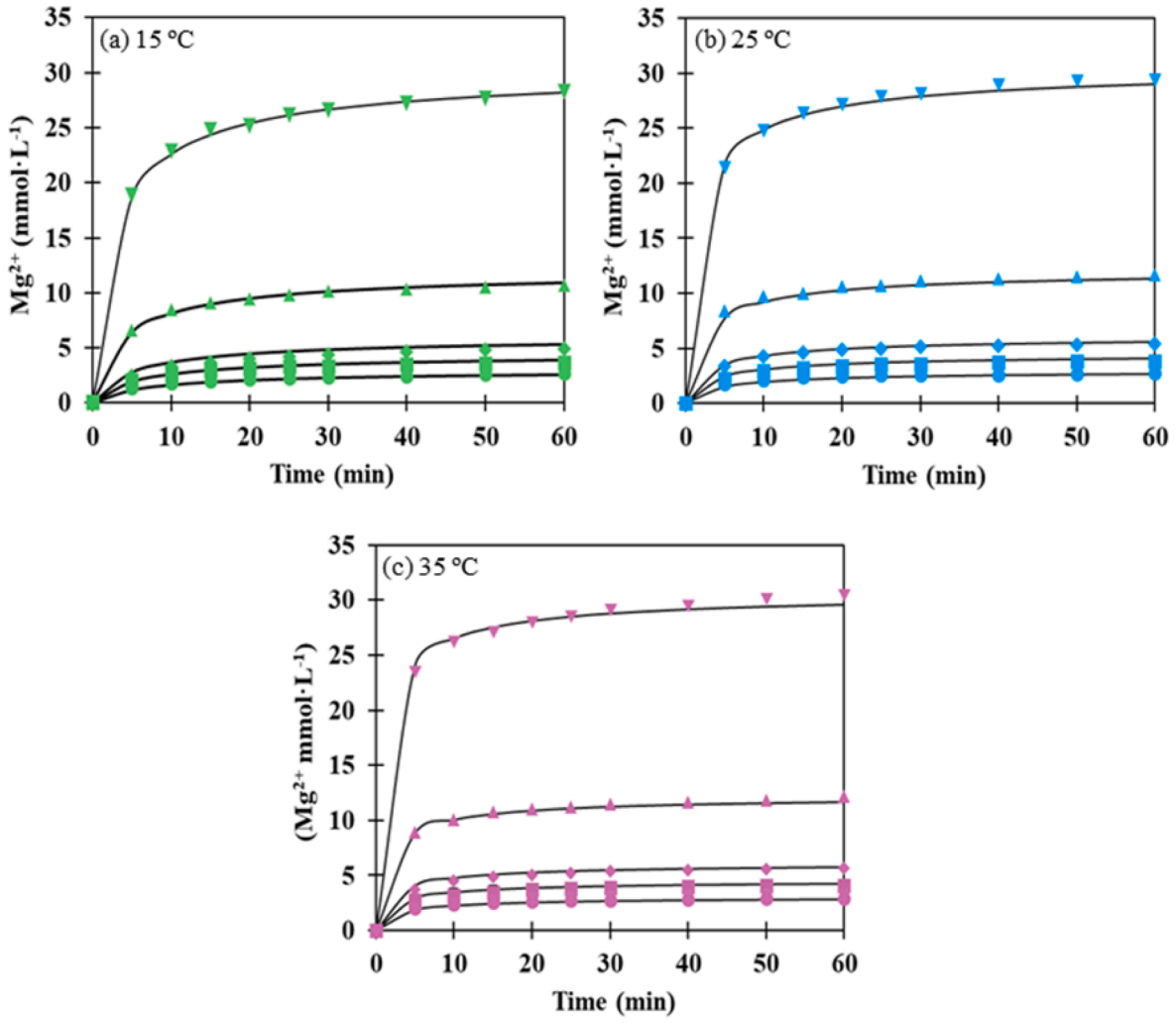

Fig. 5. Experimental Mg^{2+} concentrations (symbols) and estimated Mg^{2+} concentrations (line) at (a) 15 °C, (b) 25 °C and (c) 35 °C for each LG-MgO initial addition (●) 0.25 g·L^{-1}, (■) 0.375 g·L^{-1}, (◆) 0.50 g·L^{-1}, (▲) 1.00 g·L^{-1} and (▼) 2.50 g·L^{-1}.

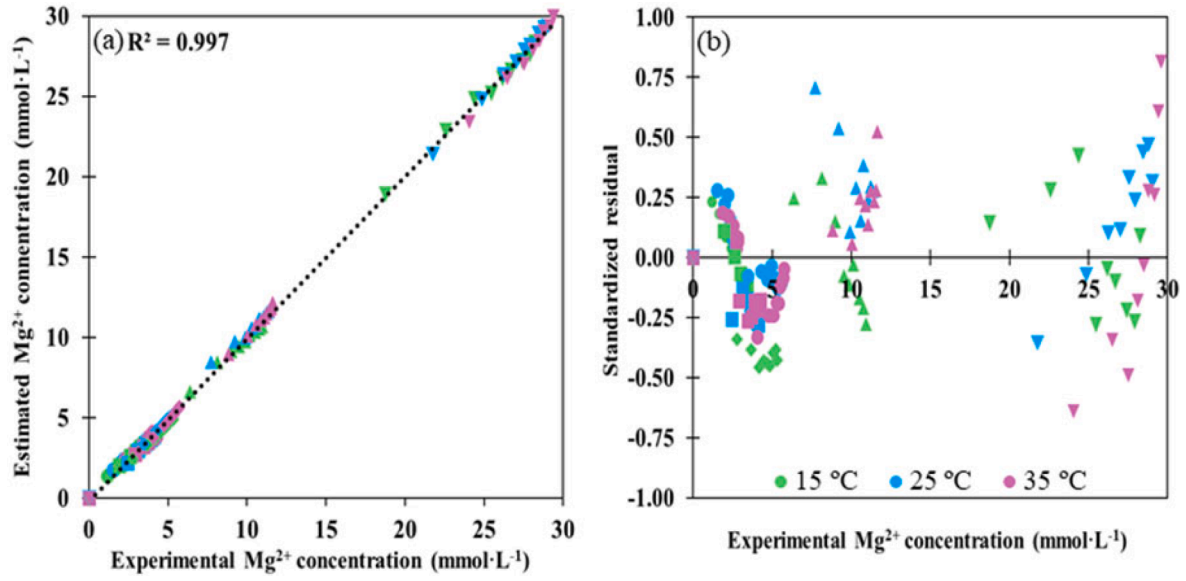

Fig. 6. (a) Experimental Mg^{2+} concentrations vs estimated Mg^{2+} concentrations where (···) is the trendline and (b) standardised residuals vs estimated Mg^{2+} concentrations. Initial LG-MgO concentration: (●) 0.25 g·L^{-1}, (■) 0.375 g·L^{-1}, (◆) 0.50 g·L^{-1}, (▲) 1.00 g·L^{-1} and (▼) 2.50 g·L^{-1}. Temperature of (●) 15 °C, (●) 25 °C and (●) 35 °C.

this initial period, the influence of temperature became progressively less relevant (Fig. 5). During the first 5 min of dissolution, the dissolved Mg^{2+} increased by 10–40 % for each 10 °C increase, depending on the initial LG-MgO concentration and the temperature. Comparatively, the corresponding increase in Mg^{2+} concentration for each 10 °C at 60 min was more limited (from 3.5 to 11.3 %). Deducible inferences from such behaviour are that the sampling during the first 5 min produces the richest values in terms of variance and function curvature, underscoring the key importance of such values in the determination of the dissolution process kinetics.

A more detailed analysis of the parity plot (Fig. 6a) shows the capability of the proposed model to predict the experimental behaviour over the full range of LG-MgO concentrations and temperatures without any particular conditions showing a poor prediction. Analysis of the standardised residuals (Fig. 6b) unveils a barely symmetrical distribution with 65 values above zero and 70 values below. The different clusters of points observed are due to the different ranges of dissolved magnesium concentrations associated with the different initial concentrations of LG-MgO. Summarising the main points from the above analysis, the main conclusion is that the proposed model is perfectly valid and suitable for the intended functionality [41,42]. This justifies its preferential application of the proposed model when compared to more complex models such as the sphere-shrinking dissolution model or the surface complexation model, as long as its use is restricted to the LG-MgO by-product.

The final estimated E_a value for the used LG-MgO was 37.5 $kJ{\cdot}mon^{-1}$, which is within the same order of magnitude but slightly slower than the previously reported values by Bugajski et al. [35], Fedoročková et al. [23] and Raschman et al. [36], which used pure MgO and followed the H^+ concentration. These authors reported E_a values of 57, 93–96 and 58 $kJ{\cdot}mol^{-1}$, respectively. Larger E_a values than those reported for pure MgO could have been expected since the citric acid test classified LG-MgO as dead-burnt [12]. The lower reactivity of LG-MgO compared to pure MgO is because LG-MgO is obtained from a high-temperature calcination process that favours the sintering of crystallites [31]. However, if explained by sintering originated from either migration and coalescence or Ostwald Ripening mechanisms at high temperatures, the lower reactivity of LG-MgO is associated with the sintered MgO crystallites of larger size. This results in lower surface area and thus slower kinetics, as can be expected from the direct relationship between surface area and dissolution rate. With respect to the reaction order, values close to 0 (0.26–0.48) were obtained in the three cited studies [23,35,36]. In this study, the estimated reaction order was 2.74, indicating that the dissolution rate is directly related to the Mg concentration in the LG-MgO and that such relation is highly non-linear with a close to cubic proportion. The mentioned studies followed a different reagent with different compositions of that herein used, which might be responsible for the different values estimated as kinetic parameters. Our close to three estimated reaction order value compares with reasonable coherence to the reaction order values of ~ 3.97 and ~ 2.00 reported for the dissolution of $MgCO_3$ and $CaMg(CO_3)_2$, respectively [41].

Bearing in mind the two step process in series conceived in the diffusion–reaction theoretical basis, it must be noted that for a surface detachment (reaction) controlled process, typical E_a values range ~40–60 $kJ{\cdot}mol^{-1}$ and (ii) $\beta > 1$ [38,43], whereas a mass transfer dominated dissolution process its characterised by E_a ranging 10–20 $kJ{\cdot}mol^{-1}$ [38,43] and β values close to the unity. Accordingly, the estimates from this work stem from a surface reaction controlled process as the most likely for the LG-MgO dissolution, which was also assumed in the model proposed by Raschman et al. [36].

4. Conclusions

Anaerobic digestion supernatant promoted the dissolution of LG-MgO, showing that it can be used as a Mg source and an alkaline reagent for struvite precipitation. The dissolved Mg^{2+} arises from MgO and $Mg(OH)_2$ in the LG-MgO instead of from the dissolution of carbonates (i.e. $MgCO_3$ and $MgCa(CO_3)_2$). Most of the magnesium contained in the LG-MgO particles was dissolved (40–78 %) in the first 5 min with a notable dependence on temperature. The developed kinetic model is simple, practical, parsimonious and specific for the by-product used. It provides excellent Mg concentration prediction capability over a wide range of conditions, as evidenced by the high global coefficients of determination ($R^2 > 0.99$) and the even and random distribution of the standardised residuals. The estimated β, A^*_0 and E_a were 2.74, 498,606 $L^{3.22}{\cdot}min^{-1}{\cdot}mmol^{-1.74}$ and 37.5 $kJ{\cdot}mol^{-1}$, respectively. These estimates underscore surface reaction as the rate limiting step for the LG-MgO dissolution process instead of the mass transfer through the interfacial boundary film layer. The resulting kinetic coefficient values from 15 to 35 °C ranged 0.079–0.219 $L^{3.22}{\cdot}min^{-1}{\cdot}mmol^{-1.74}$, respectively. The findings suggest a potential application of the simplified dissolution kinetics model as a tool for predicting the Mg^{2+} concentration and optimising the required reagent dosage.

CRediT authorship contribution statement

V.B. Aguilar-Pozo: Writing – original draft, Validation, Methodology, Investigation, Formal analysis, Conceptualization. **J.M. Chimenos:** Writing – review & editing, Supervision, Methodology, Funding acquisition, Conceptualization. **R. Soto:** Methodology, Formal analysis, Data curation, Validation, Visualization, Writing – review & editing. **C. Da Silva:** Writing – review & editing, Visualization, Validation. **P. Botines:** Writing – review & editing, Investigation. **J.F. Izquierdo:** Writing – review & editing, Validation. **S. Astals:** Writing – review & editing, Supervision, Methodology, Funding acquisition, Conceptualization.

Declaration of competing interest

The authors declare the following financial interests/personal relationships which may be considered as potential competing interests: Josep Maria Chimenos reports financial support was provided by Spain Ministry of Science and Innovation. Sergi Astals reports financial support was provided by Spain Ministry of Science and Innovation. Veronica Aguilar reports financial support was provided by Government of Catalonia Agency for Administration of University and Research Grants. Cristopher Da Silva reports financial support was provided by Government of Catalonia Agency for Administration of University and Research Grants. If there are other authors, they declare that they have no known competing financial interests or personal relationships that could have appeared to influence the work reported in this paper.

Data availability

Data will be made available on request.

Acknowledgements

This research was supported by the grant RTC2019-007257-5 funded by MCIN/AEI /10.13039/501100011033. The Agència de Gestió d'Ajuts Universitaris i de Recerca (AGAUR) de Catalunya contributed through Verónica B. Aguilar and Cristopher da Silva predoctoral grants (2022 FI_B 00032 and 2020 FISDU 00554, respectively). Sergi Astals is thankful to the Spanish Ministry of Science, Innovation and Universities for his Ramon y Cajal fellowship (RYC-2017-22372). Finally, the authors would like to thank the Catalan Government for the quality accreditation given to both research groups of the University of Barcelona (2021 SGR 00708 and 2021 SGR 00234). DIOPMA (2021 SGR 00708) is a certified agent TECNIO in the category of technology developers from the Government of Catalonia. Finally, the authors acknowledge Magnesitas Navarras S.A. for providing LG-MgO sample and CEIT-Basque Research and Technology Alliance (BRTA) and Navarra de

Infraestructuras Locales S.A. for research support.

Appendix A. Supplementary data

Supplementary data to this article can be found online at https://doi.org/10.1016/j.seppur.2024.128406.

References

[1] S. Shaddel, H. Bakhtiary-Davijany, C. Kabbe, F. Dadgar, S. Østerhus, Sustainable sewage sludge management: from current practices to emerging nutrient recovery technologies, Sustainability 11 (2019) 3435, https://doi.org/10.3390/su11123435.

[2] W.K. Wijdeveld, T. Prot, G. Sudintas, P. Kuntke, L. Korving, M.C.M. Van Loosdrecht, Pilot-scale magnetic recovery of vivianite from digested sewage sludge, Water Res. 212 (2022) 118131, https://doi.org/10.1016/j.watres.2022.118131.

[3] P.J. Talboys, J. Heppell, T. Roose, J.R. Healey, D.L. Jones, P.J.A. Withers, Struvite: a slow-release fertiliser for sustainable phosphorus management? Plant Soil 401 (2016) 109–123, https://doi.org/10.1007/s11104-015-2747-3.

[4] Q. Guan, Y. Li, Y. Zhong, W. Liu, J. Zhang, X. Yu, R. Ou, G. Zeng, A review of struvite crystallization for nutrient source recovery from wastewater, J. Environ. Manage. 344 (2023) 118383, https://doi.org/10.1016/j.jenvman.2023.118383.

[5] M. Sena, M. Seib, D.R. Noguera, A. Hicks, Environmental impacts of phosphorus recovery through struvite precipitation in wastewater treatment, J. Clean. Prod. 280 (2021) 124222, https://doi.org/10.1016/j.jclepro.2020.124222.

[6] Z. Yuan, S. Pratt, D.J. Batstone, Phosphorus recovery from wastewater through microbial processes, Curr. Opin. Biotechnol. 23 (2012) 878–883, https://doi.org/10.1016/j.copbio.2012.08.001.

[7] L. Pastor, D. Mangin, R. Barat, A. Seco, A pilot-scale study of struvite precipitation in a stirred tank reactor: Conditions influencing the process, Bioresour. Technol. 99 (2008) 6285–6291, https://doi.org/10.1016/j.biortech.2007.12.003.

[8] L. Pastor, D. Mangin, J. Ferrer, A. Seco, Struvite formation from the supernatants of an anaerobic digestion pilot plant, Bioresour. Technol. 101 (2010) 118–125, https://doi.org/10.1016/j.biortech.2009.08.002.

[9] Z. Bradford-Hartke, A. Razmjou, L. Gregory, Factors affecting phosphorus recovery as struvite: Effects of alternative magnesium sources, Desalination 504 (2021) 114949, https://doi.org/10.1016/j.desal.2021.114949.

[10] S. Vinardell, Co-digestion of sewage sludge and food waste in a wastewater treatment plant based on mainstream anaerobic membrane bioreactor technology: A techno-economic evaluation, Bioresour. Technol. 11 (2021).

[11] S.I. Lee, S.Y. Weon, C.W. Lee, B. Koopman, Removal of nitrogen and phosphate from wastewater by addition of bittern, Chemosphere 51 (2003) 265–271, https://doi.org/10.1016/S0045-6535(02)00807-X.

[12] V.B. Aguilar-Pozo, J.M. Chimenos, B. Elduayen-Echave, K. Olaciregui-Arizmendi, A. López, J. Gómez, M. Guembe, I. García, E. Ayesa, S. Astals, Struvite precipitation in wastewater treatment plants anaerobic digestion supernatants using a magnesium oxide by-product, Sci. Total Environ. 890 (2023) 164084, https://doi.org/10.1016/j.scitotenv.2023.164084.

[13] S. Astals, M. Martínez-Martorell, S. Huete-Hernández, V.B. Aguilar-Pozo, J. Dosta, J.M. Chimenos, Nitrogen recovery from pig slurry by struvite precipitation using a low-cost magnesium oxide, Sci. Total Environ. 768 (2021) 144284, https://doi.org/10.1016/j.scitotenv.2020.144284.

[14] D.-Y. Li, Y.-C. Cho, M.H. Hsu, Y.-P. Lin, Recovery of phosphate and ammonia from wastewater via struvite precipitation using spent refractory brick gravel from steel industry, J. Environ. Manage. 302 (2022) 114110, https://doi.org/10.1016/j.jenvman.2021.114110.

[15] N. Park, H. Chang, Y. Jang, H. Lim, J. Jung, W. Kim, Prediction of adequate pH and Mg 2 + dosage using an empirical MgO solubility model for struvite crystallization, Environ. Technol. Innov. 21 (2021) 101347, https://doi.org/10.1016/j.eti.2020.101347.

[16] S.R. Sakthivel, E. Tilley, K.M. Udert, Wood ash as a magnesium source for phosphorus recovery from source-separated urine, Sci. Total Environ. 419 (2012) 68–75, https://doi.org/10.1016/j.scitotenv.2011.12.065.

[17] O. Lahav, M. Telzhensky, A. Zewuhn, Y. Gendel, J. Gerth, W. Calmano, L. Birnhack, Struvite recovery from municipal-wastewater sludge centrifuge supernatant using seawater NF concentrate as a cheap Mg(II) source, Sep. Purif. Technol. 108 (2013) 103–110, https://doi.org/10.1016/j.seppur.2013.02.002.

[18] Y.-J. Shih, R.R.M. Abarca, M.D.G. de Luna, Y.-H. Huang, M.-C. Lu, Recovery of phosphorus from synthetic wastewaters by struvite crystallization in a fluidized-bed reactor: Effects of pH, phosphate concentration and coexisting ions, Chemosphere 173 (2017) 466–473, https://doi.org/10.1016/j.chemosphere.2017.01.088.

[19] M. Muys, R. Phukan, G. Brader, A. Samad, M. Moretti, B. Haiden, S. Pluchon, K. Roest, S.E. Vlaeminck, M. Spiller, A systematic comparison of commercially produced struvite: Quantities, qualities and soil-maize phosphorus availability, Sci. Total Environ. 756 (2021) 143726, https://doi.org/10.1016/j.scitotenv.2020.143726.

[20] P. Stolzenburg, A. Capdevielle, S. Teychené, B. Biscans, Struvite precipitation with MgO as a precursor: Application to wastewater treatment, Chem. Eng. Sci. 133 (2015) 9–15, https://doi.org/10.1016/j.ces.2015.03.008.

[21] A. Siciliano, C. Limonti, G.M. Curcio, Advances in struvite precipitation technologies for nutrients removal and recovery from aqueous waste and wastewater, (2020) 36.

[22] R. del Valle-Zermeño, J.M. Chimenos, J. Formosa, A.I. Fernández, Hydration of a low-grade mansium oxide. Lab-scale study, J. Chem. Technol. Biotechnol. 87 (2012) 1702–1708, https://doi.org/10.1002/jctb.3849.

[23] A. Fedoročková, P. Raschman, Effects of pH and acid anions on the dissolution kinetics of MgO, Chem. Eng. J. 143 (2008) 265–272, https://doi.org/10.1016/j.cej.2008.04.029.

[24] J.M. Chimenos, A.I. Fernández, G. Villalba, M. Segarra, A. Urruticoechea, B. Artaza, F. Espiell, Removal of ammonium and phosphates from wastewater resulting from the process of cochineal extraction using MgO-containing by-product, Water Res. 37 (2003) 1601–1607, https://doi.org/10.1016/S0043-1354(02)00526-2.

[25] M.S. Romero-Güiza, S. Astals, J. Mata-Alvarez, J.M. Chimenos, Feasibility of coupling anaerobic digestion and struvite precipitation in the same reactor: Evaluation of different magnesium sources, Chem. Eng. J. 270 (2015) 542–548, https://doi.org/10.1016/j.cej.2015.02.057.

[26] M. Quintana, M. Fco, J. Colmenarejo, G. Barrera, E. García, A.B. García, Use of a byproduct of magnesium oxide production to precipitate phosphorus and nitrogen as struvite from wastewater treatment liquors, J. Agric. Food Chem. 52 (2004) 294–299, https://doi.org/10.1021/jf0303870.

[27] V.B. Aguilar-Pozo, J.M. Chimenos, S. Peña-Picola, K. Olaciregui-Arizmendi, B. Elduayen-Echave, E. Ayesa, S. Astals, Process performance and precipitate quality of phosphorus recovery by struvite precipitation in a fluidized bed reactor using a MgO industrial by-product, J. Environ. Chem. Eng. 12 (2024) 112764, https://doi.org/10.1016/j.jece.2024.112764.

[28] M.S. Romero-Güiza, S. Tait, S. Astals, R. del Valle-Zermeño, M. Martínez, J. Mata-Alvarez, J.M. Chimenos, Reagent use efficiency with removal of nitrogen from pig slurry via struvite: A study on magnesium oxide and related by-products, Water Res. 84 (2015) 286–294, https://doi.org/10.1016/j.watres.2015.07.043.

[29] M. Quintana, M.F. Colmenarejo, J. Barrera, E. Sánchez, G. García, L. Travieso, R. Borja, Removal of phosphorus through struvite precipitation using a by-product of magnesium oxide production (BMP): Effect of the mode of BMP preparation, Chem. Eng. J. 136 (2008) 204–209, https://doi.org/10.1016/j.cej.2007.04.002.

[30] M. Quintana, E. Sánchez, M.F. Colmenarejo, J. Barrera, G. García, R. Borja, Kinetics of phosphorus removal and struvite formation by the utilization of by-product of magnesium oxide production, Chem. Eng. J. 111 (2005) 45–52, https://doi.org/10.1016/j.cej.2005.05.005.

[31] R. del Valle-Zermeño, J. Giro-Paloma, J. Formosa, J.M. Chimenos, Low-grade magnesium oxide by-products for environmental solutions: Characterization and geochemical performance, J. Geochem. Explor. 11 (2015).

[32] J. Giro-Paloma, J. Formosa, J.M. Chimenos, Stabilization Study of a Contaminated Soil with Metal(loid)s Adding Different Low-Grade MgO Degrees, (2020) 17.

[33] R.N. Goldberg, N. Kishore, R.M. Lennen, Thermodynamic Quantities for the Ionization Reactions of Buffers, J. Phys. Chem. Ref. Data 31 (2002) 231–370, https://doi.org/10.1063/1.1416902.

[34] L.F. Amaral, R. Salomão, E. Frollini, V.C. Pandolfelli, Mecanismos de hidratação do óxido de magnésio, Cerâmica 53 (2007) 368–372, https://doi.org/10.1590/S0366-69132007000400006.

[35] J. Bugajski, H. Gamsjäger, Dissolution kinetics of MgO in aqueous, acidic media, Monatshefte Für Chem. - Chem. Mon. 117 (1986) 763–772, https://doi.org/10.1007/BF00810067.

[36] P. Raschman, A. Fedoročková, Dissolution of periclase in excess of hydrochloric acid: Study of inhibiting effect of acid concentration on the dissolution rate, Chem. Eng. J. 117 (2006) 205–211, https://doi.org/10.1016/j.cej.2005.12.019.

[37] D.D. Macdonald, D. Owen, The dissolution of magnesium oxide in dilute sulfuric acid, Can. J. Chem. 49 (1971) 3375–3380, https://doi.org/10.1139/v71-561.

[38] J.W. Mullin, Crystallization, in: 4th ed., Butterworth-Heinemann, 2001: pp. 216–288.

[39] V.W. Truesdale, Batch dissolution kinetics: the shrinking sphere model with salts and its potential application to biogenic silica, Aquat. Geochem. 13 (2007) 267–287, https://doi.org/10.1007/s10498-007-9020-1.

[40] A.I. Fernández, J.M. Chimenos, M. Segarra, M.A. Fernandez, F. Espiell, Kinetic study of carbonation of MgO slurries, Hydrometallurgy (1999) 155–167.

[41] O.S. Pokrovsky, J. Schott, Surface chemistry and dissolution kinetics of divalent metal carbonates, Environ. Sci. Technol. 36 (2002) 426–432, https://doi.org/10.1021/es010925u.

[42] S. Allamsetty, S. Mohapatro, Response surface methodology-based model for prediction of NO and NO2 concentrations in nonthermal plasma-treated diesel exhaust, SN Appl. Sci. 1 (2019) 189, https://doi.org/10.1007/s42452-019-0190-4.

[43] R. Soto, Å.C. Rasmuson, Crystal growth kinetics of piracetam polymorphs in ethanol and isopropanol, Cryst. Growth Des. 19 (2019) 4273–4286, https://doi.org/10.1021/acs.cgd.8b01733.